www.MaterialsViews.com

ADVANCED
FUNCTIONAL
MATERIALS
www.afm-journal.de

FULL PAPER

Ultrathin Epitaxial Ferromagnetic γ-Fe₂O₃ Layer as High Efficiency Spin Filtering Materials for Spintronics Device Based on Semiconductors

Peng Li, Chuan Xia, Zhiyong Zhu, Yan Wen, Qiang Zhang, Husam N. Alshareef, and Xi-Xiang Zhang*

In spintronics, identifying an effective technique for generating spin-polarized current has fundamental importance. The spin-filtering effect across a ferromagnetic insulating layer originates from unequal tunneling barrier heights for spin-up and spin-down electrons, which has shown great promise for use in different ferromagnetic materials. However, the low spin-filtering efficiency in some materials can be ascribed partially to the difficulty in fabricating high-quality thin film with high Curie temperature and/or partially to the improper model used to extract the spin-filtering efficiency. In this work, a new technique is successfully developed to fabricate high quality, ferrimagnetic insulating γ-Fe₂O₃ films as spin filter. To extract the spin-filtering effect of γ-Fe₂O₃ films more accurately, a new model is proposed based on Fowler–Nordheim tunneling and Zeeman effect to obtain the spin polarization of the tunneling currents. Spin polarization of the tunneled current can be as high as −94.3% at 2 K in γ-Fe₂O₃ layer with 6.5 nm thick, and the spin polarization decays monotonically with temperature. Although the spin-filter effect is not very high at room temperature, this work demonstrates that spinel ferrites are very promising materials for spin injection into semiconductors at low temperature, which is important for development of novel spintronics devices.

1. Introduction

Injecting the spin-polarized current into semiconductors[1] efficiently is at the crux of improving spintronics devices. Thus, methods of generating highly spin-polarized currents are receiving considerable attention: two approaches have been employed to generate the spin-polarized carries.[1–3] The first uses a ferromagnetic material, such as Fe, Co, Ni, or their alloys, through which the electronic charge carriers become intrinsically spin-polarized. However, even as the source of the spin polarized current, the spin polarization in these materials is much less than 100%, where spin polarization is defined as $P = \dfrac{N_\uparrow - N_\downarrow}{N_\uparrow + N_\downarrow}$, and $N_\uparrow$ and $N_\downarrow$ denote the spin-up and spin-down electron density of states, respectively, at the Fermi level. To increase the spin polarization of the source materials, half-metallic ferromagnetic materials with fully polarized charge carriers (i.e., $P = 100\%$ of CrO₂, LaSrMnO, and Fe₃O₄, for example) have consequently been studied extensively.[4] When half-metal is used as electrode to inject spin into semiconductors, the measured spin polarization, however, is usually low. For instance, spin polarization of injected current from Fe₃O₄ into Nb:SrTiO₃ semiconductor is about 60% at 120 K[5] and 18% at 60 K.[6] The large difference between theoretical values and experimental ones comes from the large resistivity mismatch between semiconductors and half metals.[2] The second is that the nonspin polarized current from a nonmagnetic electrode becomes highly spin-polarized after tunneling through a ferromagnetic barrier (ferromagnetic insulator or ferromagnetic semiconductor)—the spin-filter effect.[7] Spin filtering has been investigated extensively as the second approach to generate spin-polarized current,[7] mainly due to the dramatic reduction in the conductivity mismatch between the tunnel barrier and the semiconductors and an increase in spin polarization. This technique has been considered the most promising approach for efficient spin injection.

An increase in spin-polarization through a spin filter takes place when electrons tunnel through a ferromagnetic insulator from a nonmagnetic metal electrode. In the conduction

Dr. P. Li, C. Xia, Y. Wen, Q. Zhang,
Prof. H. N. Alshareef, Prof. X.-X. Zhang
Division of Physical Science and Engineering
King Abdullah University of Science
and Technology (KAUST)
Thuwal 23955, Kingdom of Saudi Arabia
E-mail: xixiang.zhang@kaust.edu.sa
Dr. P. Li
Tianjin Key Laboratory of Low Dimensional
Materials Physics and Preparing Technology
Institute of Advanced Materials Physics
Faculty of Science
Tianjin University
Tianjin 300072, P. R. China
Dr. Z. Zhu
KAUST Supercomputing Laboratory (KSL)
King Abdullah University of Science & Technology (KAUST)
Thuwal 23955-6900, Kingdom of Saudi Arabia

band of a ferromagnetic insulator, spin-up and spin-down electrons encounter different tunnel barrier heights caused by the exchange-split energy. Since the tunneling probability of the electrons depends exponentially on the tunneling barrier height, the transmission probability of the tunneled spin-up and spin-down electrons are dramatically different. Therefore, the tunneled electrons should be nearly 100% spin-polarized through a ferromagnetic barrier with moderate exchange splitting, although the electron currents are zero-spin polarized before tunneling.

A number of spin filtering materials have been carefully studied for use as a tunneling barrier. Early studies focused mainly on magnetic semiconductors, such as EuS, EuSe, and EuO.[8–10] Recently, a number of ferrites with much higher Curie temperatures, $NiFe_2O_4$,[11,12] $CoFe_2O_4$,[13–15] and $MnFe_2O_4$,[16] have been studied. A spin-filtering efficiency of 23% was detected in a ferromagnetic insulating $NiFe_2O_4$-based magnetic tunneling junction (MTJ) device (LaSrMnO/STO/$NiFe_2O_4$) at 4 K.[17] Similarly, a low filtering polarization of −25% and a relatively low tunneling magnetoresistance (TMR) ratio (−18%, at 2 K) was observed in $CoFe_2O_4$-based MTJ ($CoFe_2O_4$/γ-Al_2O_3/Co).[13] Recently, an unexpectedly small positive spin-filter polarization of 9% was obtained using epitaxial $MnFe_2O_4$, whereas theoretically a negative spin-filter polarization had been predicated.[16] Potentially, the ternary nature of these compounds makes it difficult to maintain their stoichiometry. A suitable candidate may, therefore, be the binary spinel ferrite γ-Fe_2O_3, a ferrimagnetic insulator with a moderate band gap ($\approx$2.0 eV),[18] a Curie temperature of 860 K, and a calculated exchange splitting, Δ of $\approx$0.4 eV,[18] which is promising for spin filtering.

Another key issue in spintronics research is how to identify whether the highly polarized current is generated or injected. Three techniques have been commonly employed so far to extract the spin polarization or filter effect. The Meservey–Tedrow technique[19] has been used to extract spin-filter efficiency in devices where europium chalcogenides are used as the tunneling barrier: extracted filtering efficiency of 83% at 1.1 K for EuS,[8] 29% at 0.45 K for EuO,[10] and 100% at 0.45 K for EuSe.[9] Alternatively, spin-filtering efficiency could be obtained using Jullière's formula with TMR in MTJ.[11,14,17,20] Furthermore, spin light emitting diode (spin-LED) method, in which involves an electroluminescence with a quarter wavelength plate and a linear polarizer, can be used to determine the spin polarization from right and left circularly polarized light component.[21] Note that the simple Jullière model may not be adequate to derive spin polarization from a TMR value, because the effect of the decay of the wave functions of the conduction electrons in the barrier layer to the MR should be taken into account[22]; for example, in the case of a large TMR ratio observed in Fe/MgO/Fe MTJs.[22,23] Hence, the observed noisy field-dependent TMR and the puzzlingly low spin-filtering polarization in most spinel ferrite- ($NiFe_2O_4$[11,17] and $CoFe_2O_4$[13]) based sandwich heterostructures, calculated based solely on the Jullière model, may not be accurate. Interestingly, spin polarization of a ferromagnetic metal may also be obtained based on magnetic-field-dependent tunneling current through a Schottky barrier formed by a magnetic metal and a semiconductor, as demonstrated by Ziese et al.[5] on a Fe_3O_4–Nb:$SrTiO_3$ interface. In this case, the Zeeman effect caused by the

exchange splitting is tuned using a magnetic field. Although further Zeeman energy under a magnetic field ($\mu_B B$ (at 9 T) $\approx$0.52 meV) is rather small in comparison with the exchange splitting (10^{-1} eV), this idea appears to be simple and promising for detecting the efficiency of spin filters.

To address above key issues in the spin-filter devices, in this study, we show the fabrication of an ultrathin epitaxial γ-Fe_2O_3, a binary ferromagnetic insulating film that functions as a magnetic tunnel barrier with a spinel structure. Epitaxial γ-Fe_2O_3 films were fabricated by an additional oxidation of epitaxial Fe_3O_4 films on an Nb:$SrTiO_3$ substrate. To extract the spin-filtering effect more accurately, we proposed a new model based on Fowler–Nordheim tunneling and Zeeman effect. We found the spin polarization of the tunneled current to be >90 % at low temperatures using our proposed model.

2. Results and Discussion

2.1. Structural, Magnetic Characterizations and TMR

We investigated the direct growth of γ-Fe_2O_3 film on n-type semiconducting, single-crystal substrate Nb-doped $SrTiO_3$ (NSTO) by inserting a 2 nm MgO buffer layer (see Figure S1, Supporting Information). However, the insertion of an additional insulating MgO layer complicates the interface, making it more difficult to accurately determine tunneling spin-filtering efficiency. Hence, we propose an alternative approach for fabricating γ-Fe_2O_3 epitaxial films. First, high quality epitaxial Fe_3O_4 film was grown on NSTO. Then the Fe_3O_4 film was transformed to γ-Fe_2O_3 epitaxial film by annealing at high temperature in air. The quality of epitaxial Fe_3O_4 thin film was confirmed by high-resolution transmission electron microscopy (HRTEM) and an obvious Verwey transition of magnetization and resistivity at around 115 K (Figure S2, Supporting Information). To obtain high quality γ-Fe_2O_3 films, the quality epitaxial Fe_3O_4 thin films were annealed at different temperatures and for different times to find the optimized annealing condition. It was found that annealing at 300 °C for 15 min in air, Fe_3O_4 films would transform into fully relaxed γ-Fe_2O_3 films, which was demonstrated by the results obtained on a sample with 45 nm γ-Fe_2O_3 layer, as shown in **Figure 1**a. It is evident that the annealed film has same crystal structure as bulk Fe_3O_4 with a slightly shrinking of the lattice, see Figure 1a. The out-of-plane lattice constant was determined to be 8.364 Å and confirmed by the HRTEM image of the cross-sectional NSTO/γ-Fe_2O_3 in Figure 1b, which is in good agreement with the lattice constant of bulk γ-Fe_2O_3 determined as 8.347 Å by synchrotron X-ray powder diffraction.[24] The diffraction spots from NSTO and γ-Fe_2O_3 easily separate, as shown by the selected-area electron diffraction in the left inset of Figure 1b. The in-plane epitaxial structure was macroscopically demonstrated by the X-ray diffraction (XRD) ϕ scan of (111) reflection, with four identical peak intervals of 90°. The X-ray reciprocal space maps around γ-Fe_2O_3 (004) and (206) reflections were collected, as displayed in Figure 1c,d. The asymmetrical scan (206) confirms that the γ-Fe_2O_3 film is in a fully relaxed state. All of these results verified the epitaxy of γ-Fe_2O_3 films on NSTO substrates, a high quality insulating ferrimagnetic film as tunneling barrier for spin-filtering.

www.MaterialsViews.com

ADVANCED
FUNCTIONAL
MATERIALS
www.afm-journal.de

FULL PAPER
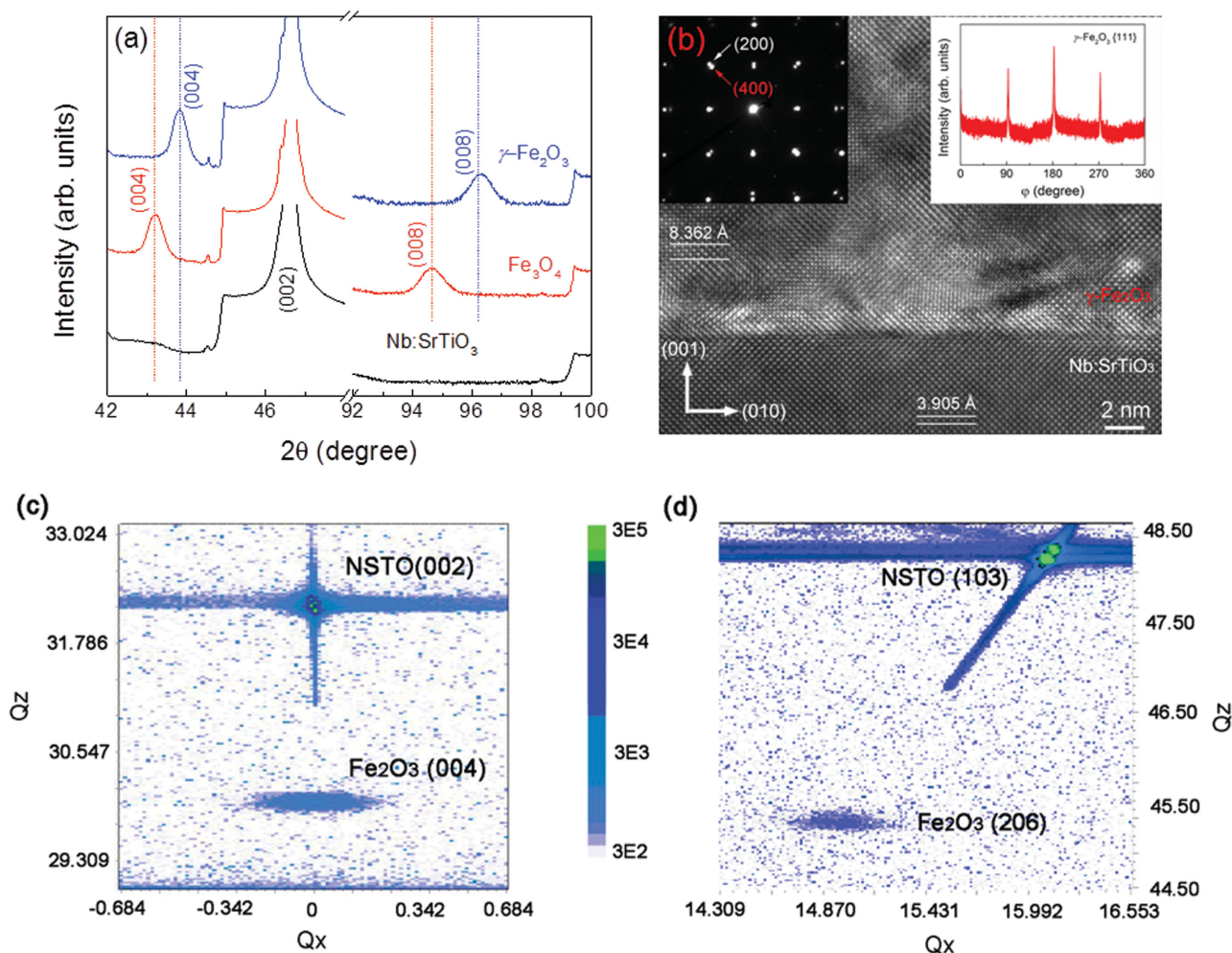
Figure 1. The structural characterization of epitaxial γ-Fe$_2$O$_3$ films. a) Comparison of XRD θ–2θ scans for bare NSTO substrate, NSTO/Fe$_3$O$_4$, and NSTO/γ-Fe$_2$O$_3$. The lattice shrinks from Fe$_3$O$_4$ to γ-Fe$_2$O$_3$. b) Cross-sectional HRTEM image of NSTO/γ-Fe$_2$O$_3$. The left inset gives the selected area electron diffraction, two sets of diffraction spots are from NSTO and γ-Fe$_2$O$_3$. The right inset shows the XRD ϕ scan of (111) reflections. X-ray reciprocal space maps around c) symmetric (002) and d) asymmetric (206) reflections for NSTO/γ-Fe$_2$O$_3$.

When the samples were annealed at a temperature over 300 °C, the magnetic properties of the resulted films would be much worse than that of γ-Fe$_2$O$_3$ films. For example, the room temperature magnetic saturation of a 45 nm film annealed 450 °C is less than 100 emu cm^{-3}, much smaller than 400 emu cm^{-3} for a sample annealed at 300 °C for 15 min (see Figure S3a, Supporting Information). Meanwhile, the XRD peak of the γ-Fe$_2$O$_3$ phase also weakened with increasing annealing temperature (Figure S3b, Supporting Information), confirming the magnetic measurements and ascribing them to the transformation of the γ-Fe$_2$O$_3$ structure into α-Fe$_2$O$_3$ structure under higher-temperature annealing. Our experimental results, including XRD and magnetization data indicate that annealing at 300 °C in air for 15 min are the optimized annealing condition to transform Fe$_3$O$_4$ films to high quality γ-Fe$_2$O$_3$ film.

The easy transformation for epitaxial Fe$_3$O$_4$ films to epitaxial γ-Fe$_2$O$_3$ films can be attributed to the fact that these two phases of Fe oxide share a similar crystalline structure, where the only difference is that the Fe^{2+} ions in Fe$_3$O$_4$ are further oxidized to Fe^{3+}. In addition, their saturation magnetization is similar if

not undistinguishable in magnetic measurements. This technique opens a new way to fabricate high quality, very thin epitaxial γ-Fe$_2$O$_3$ films, which may be applicable for other oxide films that cannot be easily grown directly.

To examine magnetic properties of the ultrathin γ-Fe$_2$O$_3$ films in the spin-filter heterostructures, we carefully subtracted the magnetic contribution of NSTO substrates, as shown in the inset of **Figure 2**a. Compared to the bulk saturation magnetization (M_S) value of 390 emu cm^{-3} (2.5 μ_B per f.u.),[25] the ultrathin films alone showed relatively high M_S values of 368, 352, 312, and 221 emu cm^{-3}, for sample thicknesses of 9.3, 6.5, 4.7, and 3.0 nm, respectively, as shown in Figure 2a. The typical temperature dependence of M_S and coercive field is shown in Figure 2b. Interestingly, although the magnetization is nearly independent of temperature over the entire temperature range, the coercive field decreased rapidly from 600 Oe at 2 K to nearly 0 Oe at 300 K. The rapid decrease of coercive field may be ascribed to the domain wall depinning as a result of thermal activation.[26]

In order to check the −100% spin filtering polarization of γ-Fe$_2$O$_3$ predicted by the band structural calculations,
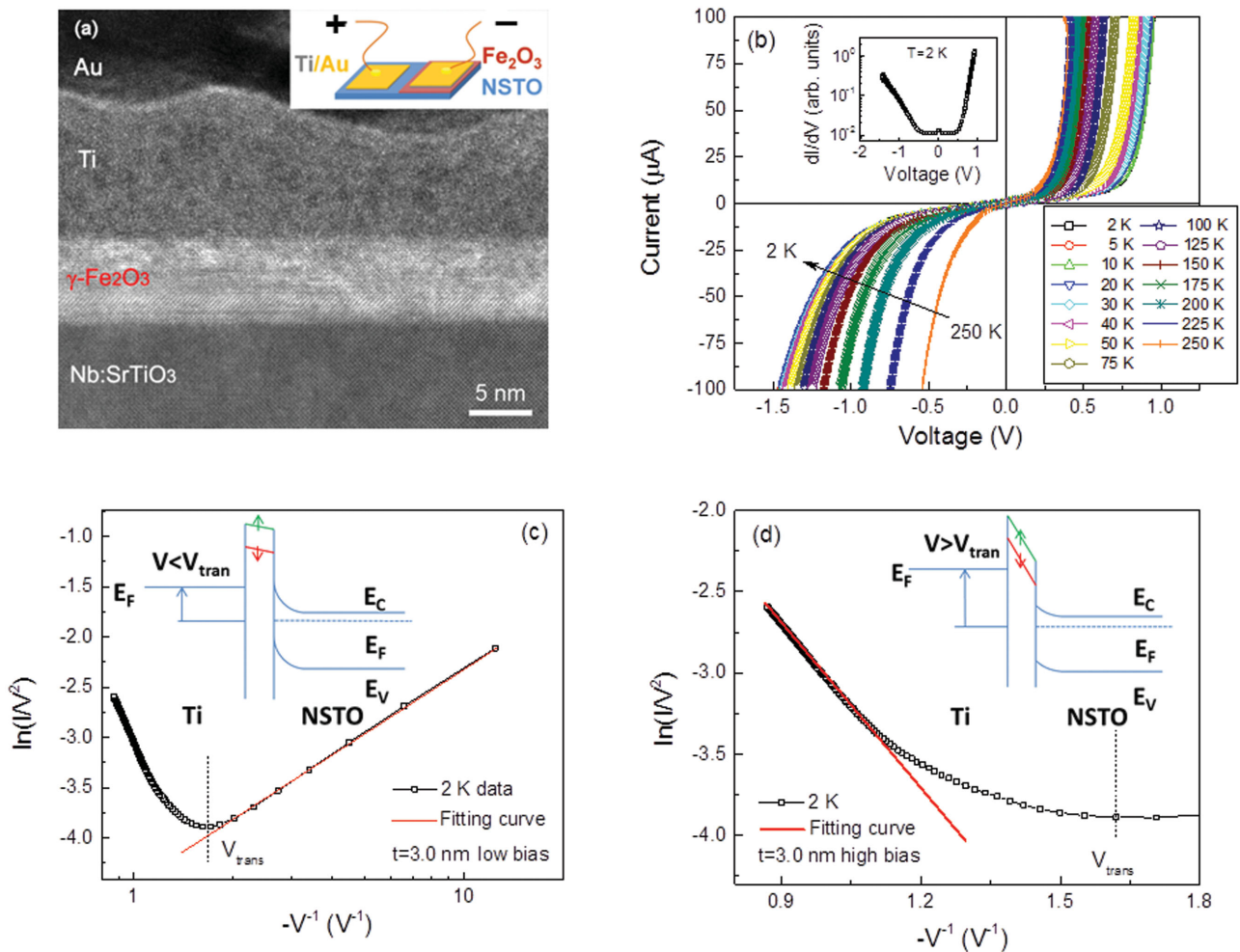
FULL PAPER
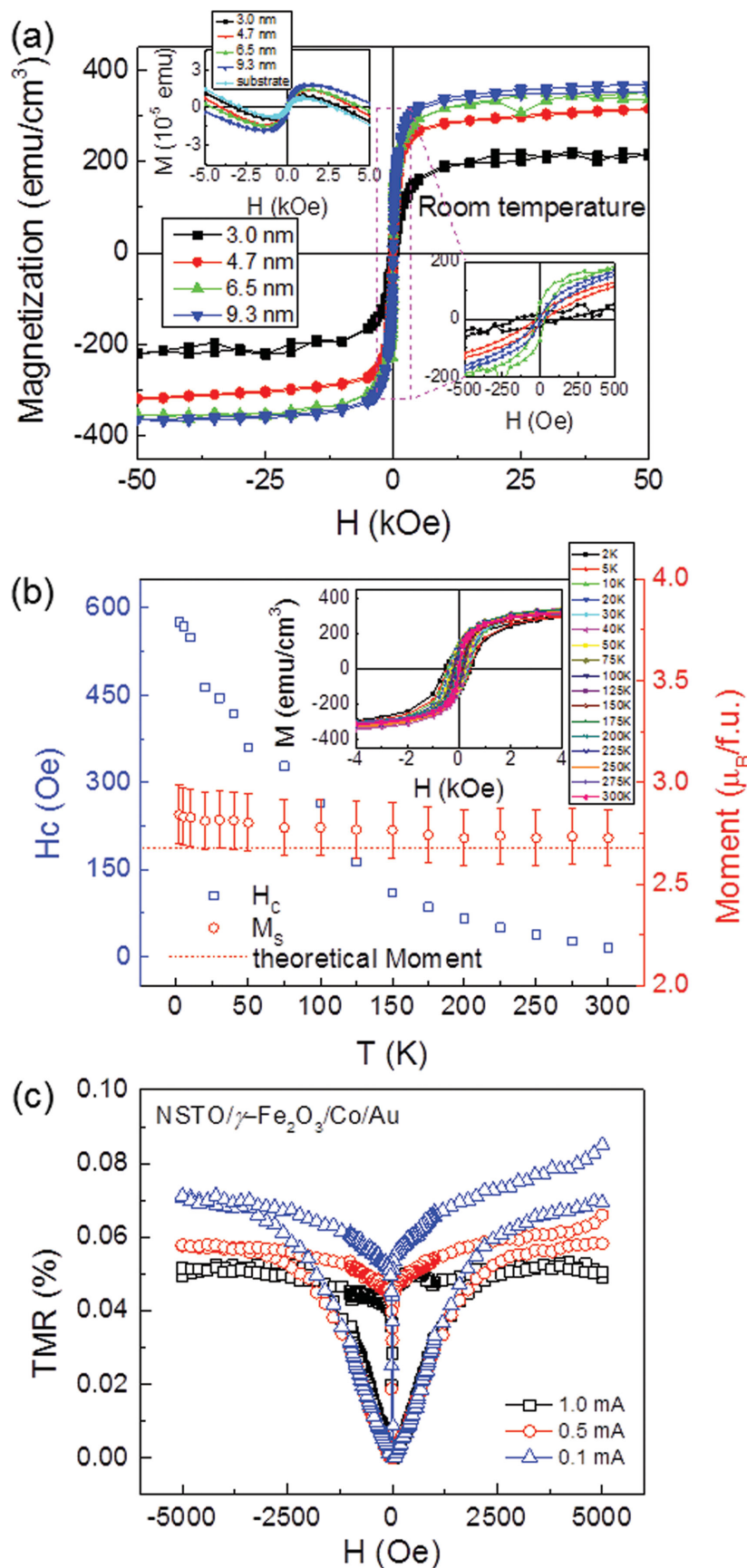
the field dependent TMR was investigated in a device of Nb:SrTiO$_3$/γ-Fe$_2$O$_3$(6.5 nm)/Co/Au. Figure 2c gives the TMR (TMR $= (R_H - R_0)/R_0$) measured at 2 K with different biases. As we expected, the positive TMR was observed in the magnetic junctions. Ascribed to the positive spin polarization of Co (40%) and negative spin filtering efficiency of γ-Fe$_2$O$_3$ (−100%) predicted by density of states (DOS) calculation, the resistance of magnetic heterostructure shows a high-resistance-state for parallel magnetization configuration (under high magnetic fields), whereas a low-resistance-state for antiparallel configuration (under zero or low magnetic fields).[27] Although the TMR behaves as we expected, its value is rather low, smaller than 0.1%. Nevertheless, the attenuation of TMR ratio with current bias in Figure 2c is exactly consistent with numerical calculation and Wentzel–Kramers–Brillouin (WKB) approximation of EuS based TMR.[28] Given to the high resistive Nb:SrTiO$_3$ electrode, the underestimated TMR ratio precludes the accurate calculation of spin-filtering polarization of γ-Fe$_2$O$_3$ from Jullière's formula. Therefore, we expect to obtain the spin-filtering polarization into semiconductors through our proposed model below.

To explore the spin-filtering effect, we first studied the electrical transport properties of Nb:SrTiO$_3$/γ-Fe$_2$O$_3$/Ti/Au samples over a wide temperature range (2–300 K) without a magnetic field. The schematic configuration of the measurements is shown in **Figure 3**a. The high quality of the heterostructured samples is evident from the HRTEM images of the cross-sections, particularly those of the epitaxial γ-Fe$_2$O$_3$ film and the interfaces in the heterostructure. Figure 3b shows the typical nonlinear $I–V$ curves measured in a wide temperature range on a sample with a 3.0 nm insulating γ-Fe$_2$O$_3$ layer. To have a closer look at the transport properties, we plotted the dI/dV versus V for the data obtained at 2 K in the inset of Figure 3b. In addition to asymmetric behavior, we observed that conductance (dI/dV) behaves very differently at different biases. The slightly asymmetric characteristic of all curves is likely caused by a bending of the

Figure 2. a) Magnetic hysteresis loops of ultrathin γ-Fe$_2$O$_3$ films at room temperature. The left upper inset provides the raw data without subtracting substrate contributions. The low field region was amplified to show the coercive field in detail. b) Temperature dependence of coercive field and saturation magnetization for 6.5 nm thick γ-Fe$_2$O$_3$ films. The inset gives all hysteresis loops at various temperatures. c) Typical magnetic field dependent TMR in Nb:SrTiO$_3$/γ-Fe$_2$O$_3$(6.5 nm)/Co/Au heterostructure with different bias at 2 K.

www.MaterialsViews.com

ADVANCED
FUNCTIONAL
MATERIALS
www.afm-journal.de

FULL PAPER

Figure 3. a) Typical cross-sectional TEM images of spin filtering heterostructure NSTO/γ-Fe$_2$O$_3$(6.5 nm)/Ti/Au. The inset shows the schematic diagram of measurement configuration. b) Typical I–V curves of heterostructures (3.0 nm γ-Fe$_2$O$_3$) recorded in a zero field at various temperatures. The inset shows the dynamic conductance dI/dV at 2 K. The tunneling transport mechanism across γ-Fe$_2$O$_3$ was determined to be c) direct tunneling and d) Fowler–Nordheim tunneling. The insets in (c) and (d) illustrate the simplified band structure.

conduction band of NSTO. The different behavior of dI/dV curves in Figure 3b is a clear indication that the tunneling mechanism changes with increasing electric bias.

By increasing the bias voltage applied across the ferromagnetic insulating barrier, the direct tunneling (DT) that dominates the properties of transport will transform into Fowler–Nordheim tunneling (FNT). Based on the WKB approximation, the current density dominated by DT and FNT can be expressed by the following equations[29]

$$J = \sqrt{2m^*\Phi}\left(\frac{e}{h}\right)^2\frac{V}{d}\exp\left[\frac{-4\pi d\sqrt{2m^*\Phi}}{h}\right] \text{and} \quad \text{DT} \tag{1}$$

$$J = \frac{e^3V^2}{8\pi\Phi hd^2}\exp\left[-\frac{d}{V}\frac{8\pi\sqrt{2m^*}}{3eh}\Phi^{\frac{3}{2}}\right], \quad \text{FNT} \tag{2}$$

where h is the Planck constant, e is the electronic charge, m^* is the effective mass of an electron, Φ is the barrier height, V is the applied bias, and d is the barrier thickness.
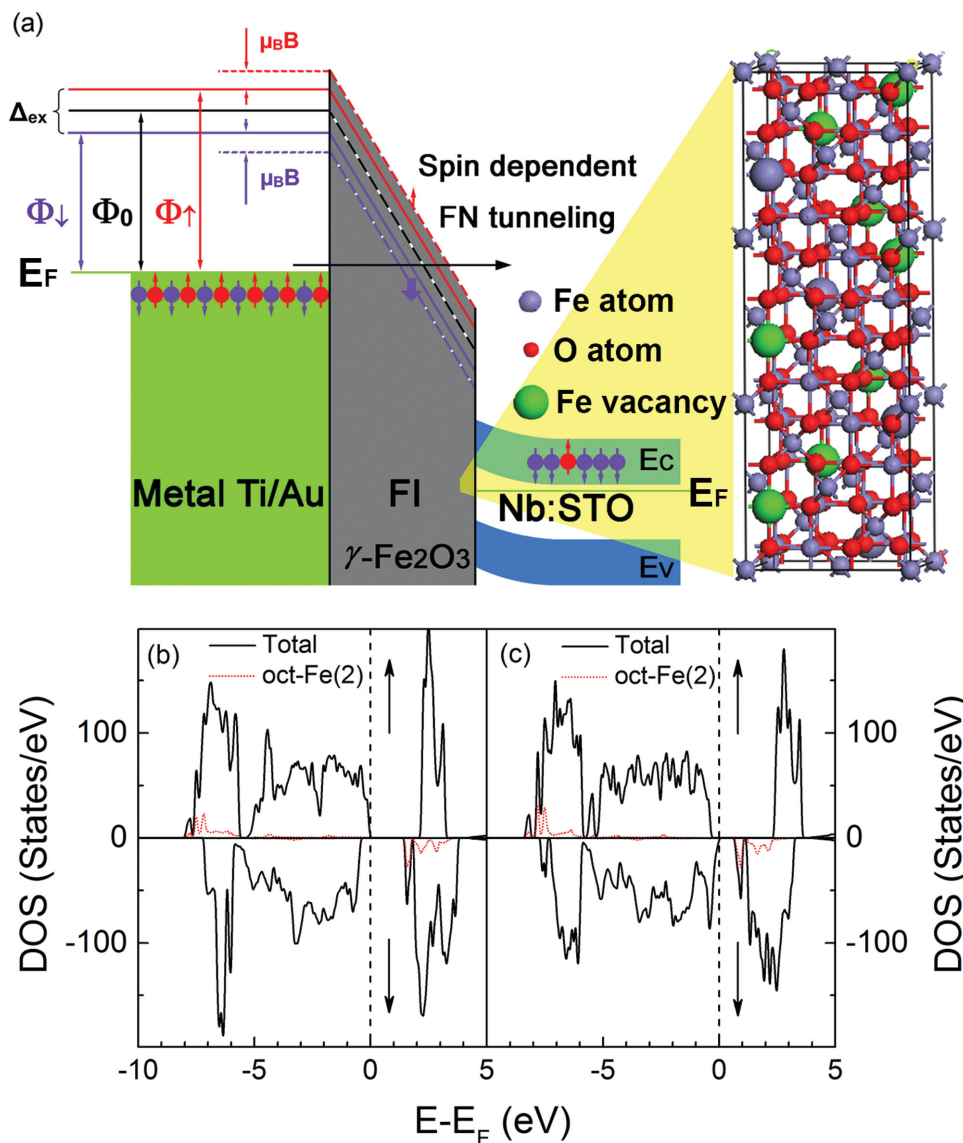
To facilitate the analysis of the behaviors/mechanisms of I–V curves, we can rewrite Equations (1) and (2) as the following

$$\ln\frac{J}{V^2} \propto \ln\frac{1}{V} - \frac{4\pi d\sqrt{2m^*\Phi}}{h} \text{ and } \quad \text{DT} \tag{3}$$

$$\ln\frac{J}{V^2} \propto -\frac{8\pi d\sqrt{2m^*}\Phi^{\frac{3}{2}}}{3eh}\left(\frac{1}{V}\right), \quad \text{FNT} \tag{4}$$

where Equations (3) and (4) represent the DT and FNT mechanisms, respectively.

For easy comparison of the experimental data between models, we replotted the data obtained at 2 K in the form of ln(I/V^2) versus 1/V as shown in Figure 3c,d. Under a low bias (Figure 3c), tunneling is dominated by the DT model, whereas under a high bias, tunneling transport is best described by the FNT mechanism (Figure 3d). As the voltage bias increases, the tunneling transport properties gradually transfer from being dominated by direct tunneling to being dominated by Fowler–Nordheim

**ADVANCED
FUNCTIONAL
MATERIALS**

www.afm-journal.de

Materials Views

www.MaterialsViews.com

FULL PAPER

Figure 4. a) The spin-filtering band structure diagram dominated by Fowler–Nordheim tunneling. The crystal structure on the right shows the ferrimagnetic insulator γ-Fe$_2$O$_3$ ($1 \times 1 \times 3$ supercell), in which the eight green balls stand for the ordered cationic vacancies. Φ_0 is the average barrier height for tunneling electrons, and Δ stands for the exchange splitting at the bottom of conduction band (purple for spin down, and red for spin up). $\mu_B B$ is the additional splitting caused by the Zeeman effect under magnetic fields. Solid and dashed lines in γ-Fe$_2$O$_3$ represent the bottom of the conduction band before and after additional Zeeman splitting. Therefore, an effective, negative spin-filtering effect can be expected. Total electronic density of states (DOS) of γ-Fe$_2$O$_3$ with DOS contributions from the second-nearest neighboring Oct-Fe, as obtained for the supercell structure b) after and c) before lattice relaxation.

tunneling at around 0.85 V. The insets of Figure 3c,d show the band structure diagram in the corresponding applied bias region.

2.2. A Spin-Filtering Model Based on the Zeeman Effect

As shown by Equations (1) and (2), the current density governed by FNT is considerably more sensitive to barrier height than is DT. This can likely be explained by the much stronger power-law dependence of the exponent on the barrier height in the faster exponential decay of the FNT model. For this reason, we will focus on spin-filtering efficiency through FN tunneling.

Taking into account the two-current model and exchange splitting (conduction band bottom of γ-Fe$_2$O$_3$ for spin down is lower than that for spin up[18]), the tunneling barrier in Equations (1) and (2) is described as $\Phi_{\uparrow(\downarrow)} = \Phi_0 + (-)\frac{\Delta}{2} + (-)\mu_B B$, in which Φ_0 is the average barrier height, Δ represents the exchange splitting of the conduction band bottom and $\mu_B B$ is the Zeeman energy; we present a schematic diagram of band structure at high voltage bias in **Figure 4**a. The crystal structure on the right shows the ferrimagnetic insulator γ-Fe$_2$O$_3$ ($1 \times 1 \times 3$ supercell), in which eight green balls stand for the ordered cationic vacancies. Φ_0 is the average barrier height for

tunneling electrons, and Δ stands for the exchange splitting at the bottom of conduction band. Based on the diagram, the ultrathin γ-Fe_2O_3 films should lead a high negative spin filtering effect. Note that energy perturbation by the Zeeman effect (on the order of 10^{-1} meV) was minimal compared to effects by Φ_0 (on the order of 10^0 eV) and Δ (on the order of 10^{-1} eV).

In the two-current model, the spin-dependent current densities are given by

$$J_{\uparrow(\downarrow)} = \frac{1}{2} J_0 \exp\left[c\Phi_{\uparrow(\downarrow)}^{\frac{3}{2}} \right] \tag{5}$$

where $J_0 = \frac{e^3 V^2}{8\pi\Phi h d^2}$ and $c = -\frac{d}{V}\frac{8\pi\sqrt{2m^*}}{3eh}$. The tunneling spin polarization is given by

$$P = \frac{J_\uparrow - J_\downarrow}{J_\uparrow + J_\downarrow} = \frac{1 - \exp\left[a\left((1-x)^{\frac{3}{2}} - (1+x)^{\frac{3}{2}} \right) \right]}{1 + \exp\left[a\left((1-x)^{\frac{3}{2}} - (1+x)^{\frac{3}{2}} \right) \right]} \tag{6}$$

where $a = c\Phi_0^{\frac{3}{2}} = -\frac{d}{V}\frac{8\pi\sqrt{2m^*}}{3eh}\Phi_0^{\frac{3}{2}}$ and $x = \frac{\Delta}{2\Phi_0} + \frac{\mu_B B}{\Phi_0}$. Using Taylor Expansion for $x < 1$, we obtain

$$(1-x)^{\frac{3}{2}} - (1+x)^{\frac{3}{2}} = -3x + \frac{x^3}{8} + \frac{3x^5}{128} + O[x]^7 \tag{7}$$

If x is small enough to ignore the cubic and high order terms in Equation (7), the spin polarization could be

$$P = \frac{J_\uparrow - J_\downarrow}{J_\uparrow + J_\downarrow} \approx \frac{1 - \exp[-3ax]}{1 + \exp[-3ax]} = \tanh\left(\frac{3}{2}ax\right) \tag{8}$$

The total current density is then given by

$$J = J_\uparrow + J_\downarrow \approx J_0 e^a \cosh\left(\frac{3}{2}ax\right) \tag{9}$$

Since $\frac{\Delta}{2} > \mu_B B$, the Taylor expansion yields

$$J = J_0 e^a \cosh\left(\frac{3a}{2}\frac{\Delta}{2\Phi_0}\right) \\ \times \left(1 + \tanh\left(\frac{3a}{2}\frac{\Delta}{2\Phi_0}\right)\frac{3a}{2}\frac{\mu_B B}{\Phi_0} + \frac{1}{2}\left(\frac{3a}{2}\frac{\mu_B B}{\Phi_0}\right)^2 \right) \tag{10}$$

Neglecting the quadratic term and taking $\left(\frac{3a}{2}\frac{\Delta}{2\Phi_0}\right) \approx \tanh\left(\frac{3a}{2}x\right) = P$, the current density ratio measured in a zero electric field and a finite magnetic field is obtained as

$$\frac{J(B)}{J(0)} \approx 1 + P\frac{3a}{2}\frac{\mu_B B}{\Phi_0} \tag{11}$$

According to Equation (11), at a constant applied bias, $I(B)/I(0)$ should be linearly dependent on the magnetic field B for a given device. Although the Zeeman energy is relatively small compared to exchange splitting, surprisingly, the slope of

$I(B)/I(0)$ to the magnetic field B will give the tunneling spin-filtering efficiency P across a ferromagnetic insulating barrier provided that the parameter a (governed by the barrier thickness, barrier height, and applied bias) is known. One may argue that the precondition to omit the x^3 and higher terms in Equation (7), for this new model, is too difficult to be satisfied. Actually, the precondition is relatively easy to be satisfied in practice. It is known that $x \approx \Delta/2\Phi < 0.5$ is valid for most ferromagnetic insulators.[9] In this case, the cubic term and high order terms in Equation (7) are at least two orders of magnitude smaller than the linear term ($-3x$), and therefore, they can be neglected safely in our model.

To demonstrate the applicability of our model to γ-Fe_2O_3 based spin filtering device, we calculated band structure of γ-Fe_2O_3. In Figure 4b, we show the total electronic DOS of the γ-Fe_2O_3 for the structure after lattice relaxation. Based on our calculations, exchange splitting was evident in γ-Fe_2O_3, with energy gaps of 2.21 and 1.89 eV for spin-up and spin-down channels, respectively, as shown in Figure 4b. We observed a coexistence of the magnetic and insulating nature, where a net total magnetization of 80 μB per supercell had energy gaps of 2.21 and 1.89 eV for spin-up and spin-down channels, respectively, which are different from the values for the position of conduction band. The bottoms of conduction band of γ-Fe_2O_3 for spin up and spin down are, respectively, 2.08 and 1.68 eV, being far away from Fermi level. The difference between the energy gaps of the two spin channels is mainly due to a localized state located inside the spin-down gap, close to the conduction states. Further investigation showed that this localized state mainly originated from the Fe atoms sitting on the second-nearest neighboring octahedral sites with respect to Fe vacancies, as shown in Figure 4b. Next, by calculating the DOS for the γ-Fe_2O_3 structure before lattice relaxation, we learned more about the nature of the magnetic insulating state of the material (see Figure 4c). Because we observed the insulating property of magnetic γ-Fe_2O_3, we can infer that the presence of the eight Oct-Fe vacancies is critical to exchange splitting. In addition, disparity between energy gaps indicates the importance of lattice distortion around the vacancies, and band structure calculations demonstrate the potential spin-filtering effect (-100%) in ferrimagnetic insulating γ-Fe_2O_3.

2.3. Tunneling Spin-Filtering Efficiency in Epitaxial Nb:SrTiO$_3$/γ-Fe$_2$O$_3$/Ti/Au

To determine tunneling spin polarization, the *I–V* curves were measured under different magnetic fields. **Figure 5**a shows the *I–V* curves measured at 2 K with applied magnetic fields varying from 0 to 9 T. Note that with increasing magnetic field, *I–V* curves shift significantly in a near parallel fashion. This type of shift can likely be explained as originating from a Zeeman effect by the magnetic insulating layer because no such shift is observed for *I–V* curves in heterostructures without an γ-Fe_2O_3 layer (see Figure 5b). A collapse of all *I–V* curves obtained under different fields (0 to 9 T), on the system without γ-Fe_2O_3 layer, into a single curve at 2 K indicates that the applied magnetic field has an unnoticeable effect on the transport properties of this system. This shift of *I–V* curves under magnetic
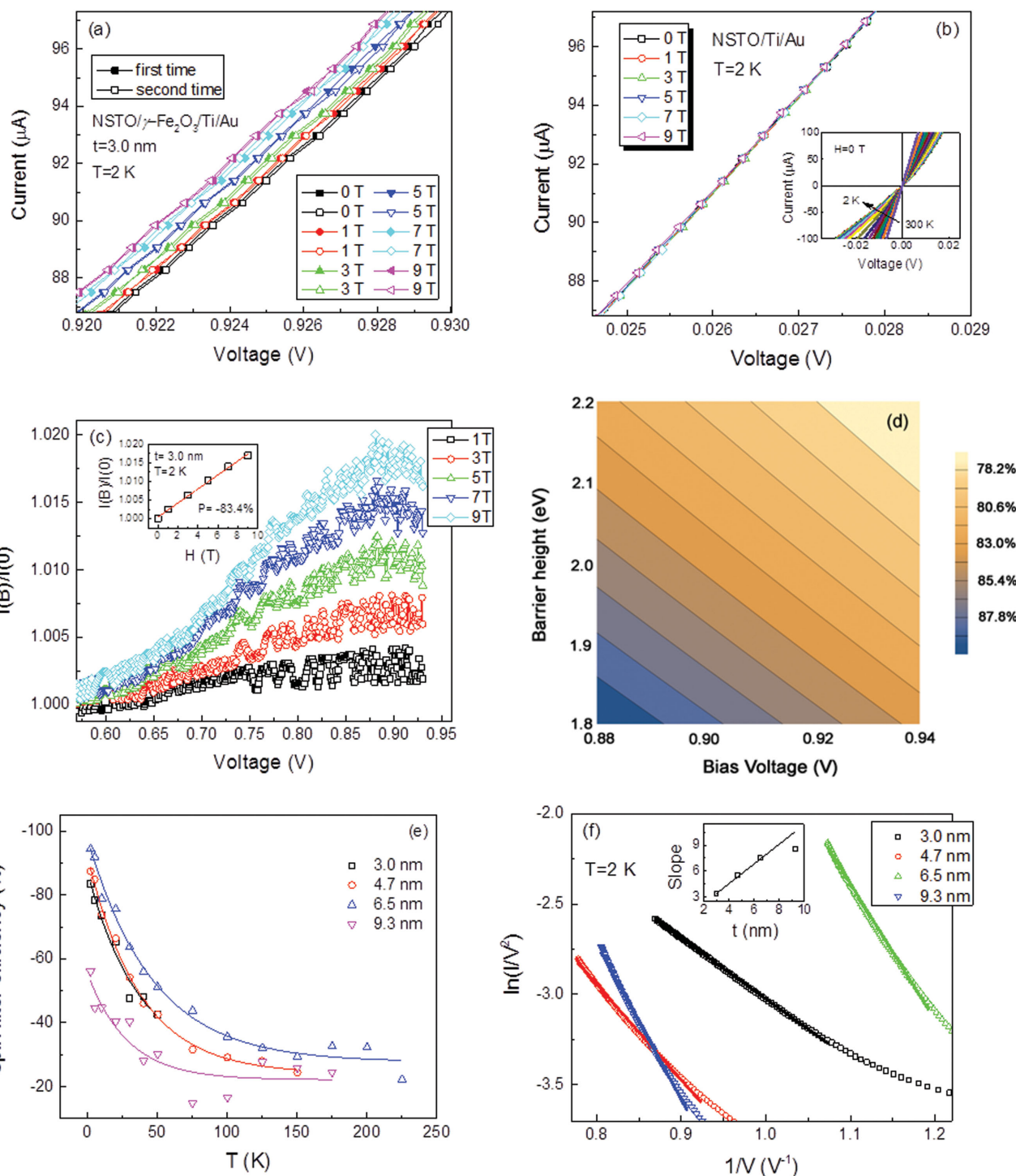
Figure 5. a) The *I–V* curves recorded twice under various magnetic fields to examine for repeatability and linear dependence. b) As a comparison, the *I–V* curves were measured in the heterostructures without ferrimagnetic insulating γ-Fe$_2$O$_3$ under various magnetic fields; no field-dependent behavior was observed within the same current range. The inset shows the nearly linear *I–V* curves measured from 2 to 300 K. c) A plot of *I*(*B*)/*I*(0) as a function of bias voltage under different magnetic fields. The typical linear slope of *I*(*B*)/*I*(0) against *B* in the inset gives the tunneling spin polarization *P* = −83.4% for a 3.0 nm sample at 2 K. d) The barrier height and bias voltage dependence of calculated spin polarization with a variation less than 5%. e) The temperature-dependent tunneling spin polarization for devices with different γ-Fe$_2$O$_3$ thicknesses. f) The curves of ln(*I*/*V*^{2}) versus 1/*V* (Fowler–Nordheim tunneling) for samples of different γ-Fe$_2$O$_3$ thicknesses. The poorest linearity is shown from the sample with 9.3 nm γ-Fe$_2$O$_3$. The inset shows how the slopes of the curves depend on the thickness of the γ-Fe$_2$O$_3$ layer, and indicates again that the sample with a 9.3 nm γ-Fe$_2$O$_3$ layer behaves different from the others.

Materials
Views
www.MaterialsViews.com

ADVANCED
FUNCTIONAL
MATERIALS
www.afm-journal.de

fields may also be explained by the Joule heating effect during measurements. To exclude the Joule heating effect on the shift of I–V curves, we measured each I–V curve twice under different magnetic fields and found that two I–V curves overlap, as shown in Figure 5a. In this experiment, a maximum current density of 7.14×10^{-3} A cm^{-2} (junction area: 1.0×1.4 mm^2) was measured, which is small enough to neglect the Joule heating effect. Therefore, we can identify the cause of the parallel shifting of I–V curves with increasing magnetic field as a consequence of the Zeeman effect from the applied magnetic field. As discussed above, governed by the Zeeman effect, $I(B)/I(0)$ in the FNT regions (high bias) should be proportional to the magnetic field. Taking 2.0 eV (the band gap of γ-Fe$_2$O$_3$) as the average barrier height Φ_0, the linear slope of $I(B)/I(0)$ against B ($V = 0.9$ V) in the inset of Figure 5c gives the tunneling spin polarization of -83.4%, as derived based on Equation (11) (note that a is a negative value), at 2 K due to the filtering effect of a 3.0 nm thick γ-Fe$_2$O$_3$ layer. The negative tunneling spin polarization agrees well with the band structure calculation.[18] To demonstrate the validity and reliability of our model, the dependences of the tunneling spin polarization on the calculated barrier height and applied bias dependence are shown in Figure 5d. Interestingly, tunneling spin polarization at 2 K for a sample with a 3.0 nm γ-Fe$_2$O$_3$ layer remains high and varies by less than 5%, despite fluctuations in Φ_0 (1.8–2.2 eV) values and/or varying bias (0.88–0.93 V) of FNT tunneling. We also fitted the dependence of normalized conductance on bias voltage obtained at 2 K on Ti/Fe$_2$O$_3$ (3.0 nm)/NSTO to Brinkman–Dynes–Rowell model to estimate the barrier height (Figure S4, Supporting Information) and found that the barrier height was ≈1.33 eV in 3.0 nm samples. If the barrier height of 1.33 eV is taken to calculate the tunneling spin polarization using Equation (11), we found that the spin polarization will be as high as -95.1% at 2 K in 3.0 nm thick sample, being much higher than spin polarization of -83.4% obtained using ideal barrier height of 2.0 eV. Therefore, the spin polarization of this device is most likely between -84% and -95%. The value (-95%) obtained with fitting barrier of ≈1.33 eV might be too high to be real, due to other nonideal factors, such as interfacial impurities, defect states, or excitation of magnons,[30] that may deteriorate the efficiency. Finally, we measured the I–V curves using the same technique to explore how tunneling spin polarization depends on the thickness of the magnetic insulating layer and on the temperature. Figure 5e shows the tunneling spin polarization obtained on samples with different γ-Fe$_2$O$_3$ thicknesses at various temperatures. It is evident that high-spin-filter efficiency can be achieved at low temperatures with an appropriately thick γ-Fe$_2$O$_3$ layer. Samples with γ-Fe$_2$O$_3$ layers with thickness between 3.0 and 4.7 nm have efficiencies as high as -84% at 2 K or up to -94.3% for samples with a 6.5 nm γ-Fe$_2$O$_3$ layer. The enhancement of spin polarization with increasing thickness of γ-Fe$_2$O$_3$ layer from 3.0 to 6.5 nm might be ascribed to the increase of magnetization in thicker films (Figure 2a). However, markedly reduced spin filter efficiency was observed with 9.3 nm γ-Fe$_2$O$_3$ layers and with increasing temperature. For example, efficiency dropped from -94% to less than -40% as temperature increased from 2 to 200 K for the 6.5 nm sample.

Figure 5e clearly illustrates how the spin-filter efficiency is enhanced with increasing layer thickness up to 6.5 nm because of the enhanced magnetization in thicker films (Figure 3b). The decrease in spin polarization at 9.3 nm sample might be due to the fact that the tunneling barrier becomes too thick. Consequently, a nonideal FNT mechanism is expected, making the model inapplicable to samples with too thick tunneling layer, which is evidenced by the poorer linearity of $\ln(I/V^2)$ versus $1/V$ of the 9.3 nm sample than that of other samples in the high-bias region (Figure 5f). Based on Equation (11), the correlation between the thickness and barrier can be obtained from the value of the slope. Thus, we plotted the dependence of the slope (absolute values) on the thickness of the γ-Fe$_2$O$_3$ layer in the inset of Figure 5f. A deviation from linear dependence is evident for the 9.3 nm sample, indicating that the FN tunneling model may not appropriately describe the behavior of I–V in samples with a thicker barrier layer. For a deeper understanding of the behavior of the 9.3 nm sample, we analyzed the surface of γ-Fe$_2$O$_3$ films of different thicknesses using atomic force microscopy. The results indicate that the average roughness of γ-Fe$_2$O$_3$ is less than that for Fe$_3$O$_4$ layer, except for the 9.7 nm sample (see Figure S5, Supporting Information). Therefore, surface roughness may also contribute to the low-tunneling spin polarization and deviations from FN tunneling behavior.

One should also note that when temperatures increased above 225 K, a rapid decrease in tunneling spin polarization accompanied by a complete loss of linear dependence of $I(B)/I(0)$ on magnetic field was observed in the samples with ultrathin γ-Fe$_2$O$_3$ layers. This may be understood as following. At 250 K, the thermal energy, k_BT ≈20.83 meV, is comparable to the magnetocrystalline anisotropy energy (≈20 meV) for a single-antiphase domain, if we take 10 nm as the typical antiphase domain size[31] in epitaxial ferrite films with thickness less than 10 nm ($K_{eff}V$, 10 nm × 10 nm × 6.5 nm, bulk K_{eff}:[32] 4.7×10^4 erg cm^{-3}). Apparently, thermal agitation, when the temperature is above 250 K, is sufficient to cause reversals of the magnetic moment of the domain in the epitaxial γ-Fe$_2$O$_3$ layer. Subsequently, the spin-filtering effect disappeared at high temperatures in our macroscopic samples (1 mm × 1 mm). In contrast, owing to the large anisotropy constant of CoFe$_2$O$_4$,[33] K ≈3.0×10^6 erg cm^{-3}, spin filtering was achieved at room temperature in samples where a CoFe$_2$O$_4$ layer acts as the spin filter based on Julliere's formula.[13] Actually, the decreased conceive field in NiFe$_2$O$_4$ films is also considered being responsible for the loss of spin filtering effect as the temperature increases.[11] Nevertheless, the tunneling spin polarization reached -30% even at temperatures as high as 200 K, making γ-Fe$_2$O$_3$ a more effective spin filter than other ferrites (e.g., NiFe$_2$O$_4$,[11] CoFe$_2$O$_4$,[13,14] and MnFe$_2$O$_4$[16]).

3. Conclusions

In summary, we have developed a new technique to fabricate high quality γ-Fe$_2$O$_3$ layer for spin-filtering by transforming the epitaxial Fe$_3$O$_4$ films. With γ-Fe$_2$O$_3$ layer as a filter, we have achieved high spin-filtering efficiency, e.g., >94% in an optimized sample at 2 K. This work clearly demonstrated that γ-Fe$_2$O$_3$ are very

FULL PAPER

promising as spin filtering materials for the fundamental research and possible applications. The growth technique of high quality γ-Fe$_2$O$_3$ films may also be extended to other oxide thin films.

We have also proposed a new model to determine tunneling spin polarization in TMR devices more properly. This model is different from the existing Meservey–Tedrow's dynamic conductance model, Julliere's two-channel conduction model, and spin-LED method. Based on this model, the tunneling spin polarization can be obtained reliably in spite of an unknown exchange splitting Δ value (normally it is not easy to obtain detailed information on splitting), by using the thickness of the tunneling barrier layer, the barrier height, and the electric bias applied to the FNT region.

4. Experimental Section

Sample Fabrication: The epitaxial Fe$_3$O$_4$ on Nb(0.7%):SrTiO$_3$ (001) was fabricated by reactive sputtering from pure Fe targets (99.95%). The Fe$_3$O$_4$ layers with thickness between 3.0 and 9.7 nm were deposited at 700 °C on Nb:SrTiO$_3$ with an oxygen partial pressure of 2.5×10^{-5} mbar. Thermal annealing in an ambient atmosphere transformed Fe$_3$O$_4$ into metastable γ-Fe$_2$O$_3$. The best annealing temperature was determined to be 300 °C (see Figure S3, Supporting Information). A layer of SiN$_x$ (300 nm) by plasma-enhanced chemical vapor deposition at 150 °C was patterned using the lift-off method to provide an electrically isolated contact window on top of the junctions. The upper electrode Ti (10 nm)/Au (200 nm) deposition was followed by sputtering and the residual photoresist AZ5214 was removed by oxygen plasma before deposition.

Characterization of Structure and Physical Properties: The epitaxial structure of γ-Fe$_2$O$_3$ was confirmed by high-resolution X-ray diffraction (Bruker diffractometer D8 Discover) and HRTEM (Titan 80300 kV (ST) TEM, FEI). The chemical state was confirmed by X-ray photoelectron spectrum, as shown in Figure S6 (Supporting Information). Thickness was determined by HRTEM and confirmed by Rutherford backscattering spectrometry, as shown in Figure S7 (Supporting Information). The roughness of the ultrathin films was checked by atomic force microscopy, as shown in Figure S5 (Supporting Information). The magnetic properties of γ-Fe$_2$O$_3$ with contributions by the substrate subtracted were obtained using a Quantum Design magnetic property measurement system (SQUID-VSM). The I–V curves by two terminals (Nb:SrTiO$_3$: negative, Ti/Au: positive) were measured with a physical property measurement system (PPMS-9, Quantum Design). We removed the Joule heating effect by limiting the maximum current to 100 µA and the minimum waiting-time interval to 30 s between the two I–V curves. In our experiments, we measured three different samples for each kind shaped by standard lithography method.

Calculation Method: To expand our understanding of the spin-split band gap of γ-Fe$_2$O$_3$, we performed full-potential linearized augmented plane-wave calculations using the WIEN2K package. For a strong correlation effect, DFT+U method was used with the U parameter for Fe d electrons (4 eV), as explained in ref. [29]. To simulate γ-Fe$_2$O$_3$, a $1 \times 1 \times 3$ supercell based on the cubic spinel structure of Fe$_3$O$_4$ was built, where eight Fe vacancies were created in the lowest energy configuration, as reported in ref. [23]. This results in a structure with the space group P4$_1$2$_1$2 and lattice constants $a = 8.364$ Å, $b = 8.364$ Å, and $c = 25.092$ Å, in which there are 64 Fe atoms and 96 O atoms. We set the R_{mt} of Fe and O to 2.2 a.u. and 1.2 a.u., respectively. Due to the much smaller radius of O, a smaller $R_{mt}K_{max}$ of 4.5 was used. An identical $6 \times 6 \times 2$ k-mesh was used in all calculations. The atoms in the structure were fully relaxed with a force tolerance of 1.0 mRy per Bohr, and Pulay corrections were implemented into the force calculations. Generalized gradient approximations to the exchange-correlation function in the Perdew Burk Erezerhof form was employed to both optimize the lattice and structure electronic calculations.

[1] Y. Ohno, D. K. Young, B. Beschoten, F. Matsukura, H. Ohno, D. D. Awschalom, *Nature* **1999**, *402*, 790.

[2] G. Schmidt, D. Ferrand, L. W. Molenkamp, A. T. Filip, B. J. van Wees, *Phys. Rev. B* **2000**, *62*, R4790.

[3] P. LeClair, J. K. Ha, H. J. M. Swagten, J. T. Kohlhepp, C. H. van de Vin, W. J. M. de Jonge, *Appl. Phys. Lett.* **2002**, *80*, 625.

[4] a) S. Jin, M. Mccormack, T. H. Tiefel, R. Ramesh, *J. Appl. Phys.* **1994**, *76*, 6929; b) H. Y. Hwang, S. W. Cheong, *Science* **1997**, *278*, 1607; c) J. M. D. Coey, C. L. Chien, *MRS Bull.* **2003**, *28*, 720.

[5] M. Ziese, U. Kohler, A. Bollero, R. Hohne, P. Esquinazi, *Phys. Rev. B* **2005**, *71*, 180406R.

[6] Y. Z. Chen, J. R. Sun, Y. W. Xie, D. J. Wang, W. M. Lu, S. Liang, B. G. Shen, *Appl. Phys. Lett.* **2007**, *90*, 143508.

[7] J. S. Moodera, T. S. Santos, T. Nagahama, *J. Phys.: Condens. Matter* **2007**, *19*, 165202.

[8] J. S. Moodera, X. Hao, G. A. Gibson, R. Meservey, *Phys. Rev. Lett.* **1988**, *61*, 637.

[9] J. S. Moodera, R. Meservey, X. Hao, *Phys. Rev. Lett.* **1993**, *70*, 853.

[10] T. S. Santos, J. S. Moodera, *Phys. Rev. B* **2004**, *69*, 241203.

[11] U. Luders, M. Bibes, K. Bouzehouane, E. Jacquet, J. P. Contour, S. Fusil, J. F. Bobo, J. Fontcuberta, A. Barthelemy, A. Fert, *Appl. Phys. Lett.* **2006**, *88*, 082505.

[12] E. Negusse, J. Holroyd, M. Liberati, J. Dvorak, Y. U. Idzerda, T. S. Santos, J. S. Moodera, E. Arenholz, *J. Appl. Phys.* **2006**, *99*, 08e507.

[13] A. V. Ramos, M. J. Guittet, J. B. Moussy, R. Mattana, C. Deranlot, F. Petroff, C. Gatel, *Appl. Phys. Lett.* **2007**, *91*, 122107.

[14] Y. K. Takahashi, S. Kasai, T. Furubayashi, S. Mitani, K. Inomata, K. Hono, *Appl. Phys. Lett.* **2010**, *96*, 072512.

[15] a) C. Xia, H. N. Alshareef, *Chem. Mater.* **2015**, *27*, 4661; b) C. Xia, W. Chen, X. B. Wang, M. N. Hedhili, N. N. Wei, H. N. Alshareef, *Adv. Energy Mater.* **2015**, *5*, 1401805; c) C. Xia, P. Li, A. N. Gandi, U. Schwingenschlogl, H. N. Alshareef, *Chem. Mater.* **2015**, *27*, 6482; d) C. Xia, Q. Jiang, C. Zhao, M. N. Hedhili, H. N. Alshareef, *Adv. Mater.* **2016**, *28*, 77.

[16] S. Matzen, J. B. Moussy, G. X. Miao, J. S. Moodera, *Phys. Rev. B* **2013**, *87*, 184422.

[17] U. Luders, A. Barthelemy, M. Bibes, K. Bouzehouane, S. Fusil, E. Jacquet, J. P. Contour, J. F. Bobo, J. Fontcuberta, A. Fert, *Adv. Mater.* **2006**, *18*, 1733.

[18] R. Grau-Crespo, A. Y. Al-Baitai, I. Saadoune, N. H. De Leeuw, *J. Phys.: Condens. Matter* **2010**, *22*, 255401.

ADVANCED
FUNCTIONAL
MATERIALS
www.afm-journal.de

www.MaterialsViews.com

FULL PAPER

[19] a) P. M. Tedrow, R. Meservey, *Phys. Rev. Lett.* **1971**, *26*, 192; b) P. M. Tedrow, R. Meservey, *Phys. Rev. B* **1973**, *7*, 318.

[20] a) M. Gajek, M. Bibes, A. Barthelemy, K. Bouzehouane, S. Fusil, M. Varela, J. Fontcuberta, A. Fert, *Phys. Rev. B* **2005**, *72*, 020406; b) Y. H. Liu, F. A. Cuellar, Z. Sefrioui, J. W. Freeland, M. R. Fitzsimmons, C. Leon, J. Santamaria, S. G. E. te Velthuis, *Phys. Rev. Lett.* **2013**, *111*, 247203.

[21] E. Wada, K. Watanabe, Y. Shirahata, M. Itoh, M. Yamaguchi, T. Taniyama, *Appl. Phys. Lett.* **2010**, *96*, 102510.

[22] J. Mathon, A. Umerski, *Phys. Rev. B* **2001**, *63*, 220403.

[23] a) S. S. P. Parkin, C. Kaiser, A. Panchula, P. M. Rice, B. Hughes, M. Samant, S. H. Yang, *Nat. Mater.* **2004**, *3*, 862; b) S. Yuasa, T. Nagahama, A. Fukushima, Y. Suzuki, K. Ando, *Nat. Mater.* **2004**, *3*, 868.

[24] J. E. Jorgensen, L. Mosegaard, L. E. Thomsen, T. R. Jensen, J. C. Hanson, *J. Solid State Chem.* **2007**, *180*, 180.

[25] H. Yanagihara, M. Hasegawa, E. Kita, Y. Wakabayashi, H. Sawa, K. Siratori, *J. Phys. Soc. Jpn.* **2006**, *75*, 054708.

[26] X. X. Zhang, J. M. Hernandez, J. Tejada, R. Sole, X. Ruiz, *Phys. Rev. B* **1996**, *53*, 3336.

[27] K. Ghosh, S. B. Ogale, S. P. Pai, M. Robson, E. Li, I. Jin, Z. W. Dong, R. L. Greene, R. Ramesh, T. Venkatesan, M. Johnson, *Appl. Phys. Lett.* **1998**, *73*, 689.

[28] T. Nagahama, T. S. Santos, J. S. Moodera, *Phys. Rev. Lett.* **2007**, *99*, 016602.

[29] a) M. Lenzling, E. H. Snow, *J. Appl. Phys.* **1969**, *40*, 278; b) M. Muller, G. X. Miao, J. S. Moodera, *EPL* **2009**, *88*, 47006.

[30] T. S. Santos, J. S. Moodera, K. V. Raman, E. Negusse, J. Holroyd, J. Dvorak, M. Liberati, Y. U. Idzerda, E. Arenholz, *Phys. Rev. Lett.* **2008**, *101*, 147201.

[31] W. Eerenstein, T. T. M. Palstra, T. Hibma, S. Celotto, *Phys. Rev. B* **2003**, *68*, 014428.

[32] B. Martinez, A. Roig, X. Obradors, E. Molins, A. Rouanet, C. Monty, *J. Appl. Phys.* **1996**, *79*, 2580.

[33] H. Yanagihara, K. Uwabo, M. Minagawa, E. Kita, N. Hirota, *J. Appl. Phys.* **2011**, *109*, 07c122.